Analysis of fast-ion D_α data from the National Spherical Torus Experiment

Analysis of fast-ion D_α data from the National Spherical Torus Experiment

W.W. Heidbrink[1]**, E. Ruskov**[1]**, D. Liu**[1]**, L. Stagner**[1]**, E.D. Fredrickson**[2]**, M. Podestà**[2] **and A. Bortolon**[2]

[1] University of California Irvine, Irvine, CA 92697, USA
[2] Princeton Plasma Physics Laboratory, Princeton, NJ 08540, USA

E-mail: Bill.Heidbrink@uci.edu

CrossMark

Abstract

Measured fast-ion D_α (FIDA) data from an extensive NSTX database are compared to 'classical' predictions that neglect transport by instabilities. Even in the absence of appreciable MHD, in many cases, the profile peaks at smaller major radius and the profile is broader than the predictions. Abrupt large-amplitude MHD events flatten the FIDA profile, as do most toroidal Alfvén eigenmode (TAE) avalanche events. Generally, the onset of a long-lived mode also flattens the FIDA profile.

Keywords: Alfvén eigenmodes, energetic particles, spherical tokamak

(Some figures may appear in colour only in the online journal)

1. Introduction

The National Spherical Torus Experiment (NSTX) was a low-field, spherical tokamak with intense neutral-beam heating. Instabilities driven by fast ions were often observed because the beam ions were super-Alfvénic and the fast-ion pressure was relatively large. In a recent study, Fredrickson *et al* [1] created a database of NSTX discharges to assess the parametric dependences of the various types of observed MHD. Classified instabilities included

- abrupt large-amplitude events (ALE) resembling those observed on JT-60 [2],
- steady or regularly bursting modes in the toroidal Alfvén eigenmode (TAE) range of frequencies [3, 4],
- TAE avalanches [5],
- high-frequency global [6] and compressional [7] Alfvén eigenmodes (GAEs, CAEs), including GAE avalanches [8],
- frequency-chirping energetic particle modes (EPM) [9, 10] that often terminate in long-lived modes (LLMs) similar to those observed on MAST [11], and
- MHD-quiescent plasmas.

In their study, Fredrickson *et al* studied the effect of the various instabilities on the neutron rate but did not consider any other fast-ion data. Despite recent progress [5, 12–15], the available information about fast-ion profiles in spherical tokamaks is still rather limited.

NSTX was equipped with a 16-channel vertically-viewing FIDA diagnostic [16] that collected data for the same discharges as were analyzed in [1]. The purpose of the present study is to analyze these data to glean additional information on the effect of the different instabilities on the fast-ion profile. After an introduction to the instrument and the analysis techniques (section 2), evidence is presented that the FIDA profiles deviate from theoretical predictions even in the absence of detectable MHD (section 3). Section 4 considers the effect of different types of MHD. Conclusions are drawn in section 5.

2. Apparatus and analysis techniques

The data are from deuterium discharges from the 2010 NSTX campaign with a central electron temperature of $T_e = 0.54$–1.5 keV, central electron density of $n_e = 1.0$–8.6×10^{19} m^{-3}, edge safety factors of $q_{95} = 6$–43, effective charge $Z_{eff} = 1.2$–5.6, major radius of the magnetic axis $R_0 = 95$–108 cm, toroidal field $B_T = 0.21$–0.48 T and plasma current $I_p = 0.30$-1.1 MA. Deuterium neutral beam heating with injected power of $P_B = 1.5$–6.1 MW is employed. The injection energy is usually 90 keV, although it is 65 keV on some shots. Three sources
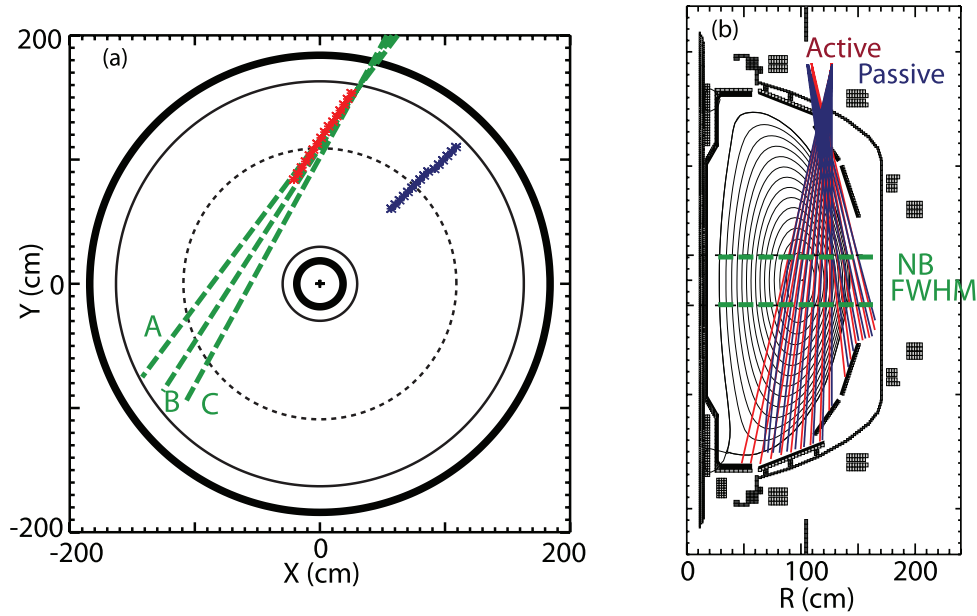
Figure 1. (*a*) Plan view and (*b*) elevation of the NSTX vessel showing the locations of the active and passive FIDA views. The centerlines and vertical full widths at half-maximum (FWHM) of the three neutral beam sources are also shown (thick dashed lines). The magnetic axis (dotted line) and radii of the last closed flux surface (thin solid lines) at the midplane for a typical discharge are also shown.
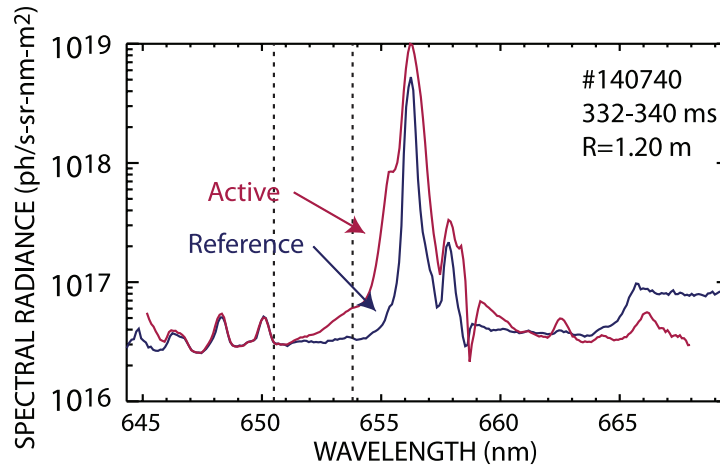

Figure 2. FIDA spectra from active and passive FIDA views. The dotted vertical lines indicate the spectral range employed in the spectral and profile fitting.

(called 'A', 'B' and 'C') inject in the direction of the plasma current with tangency radii of 69, 59 and 50 cm.

FIDA is a type of charge exchange recombination spectroscopy that exploits the large Doppler shift of light emitted by fast ions that neutralize in an injected beam to infer properties of the fast-ion distribution function [17]. The geometry of the NSTX FIDA measurement is shown in figure 1. Arrays of fibers view source B from a vertical port that is aligned with the beam. All three sources inject into the plasma through the same midplane port, so sources A and C also contribute to the active signal. The angle of the sightline relative to the magnetic field ranges from ∼90° at the magnetic axis to ∼70° at the plasma edge for typical conditions. Another array of toroidally displaced fibers provide reference views. After dispersion by a spectrometer, 16 active spectra and 16 passive

spectra are acquired by a single CCD camera [16]. The integration time for the camera is 10 ms but, to avoid blurring, the light is blocked during readout for ∼1.8 ms of each time window.

Typical spectra for one channel appear in figure 2. The rest wavelength for the Balmer alpha transition is at 656.1 nm. The apparatus attenuates the cold line to avoid camera saturation. Between 650 and 662 nm, the active signal is larger than the reference signal; away from the cold line, this difference is attributed to FIDA emission caused by interaction of injected neutrals with confined fast ions. Impurity emission, such as the oxygen line at 650.24 nm, also contributes to the signal. Because the ion temperature is ≲1 keV in most of these plasmas, the FWHM of the light produced by thermal atoms in the halo is ≲1.0 nm, so the thermal feature makes
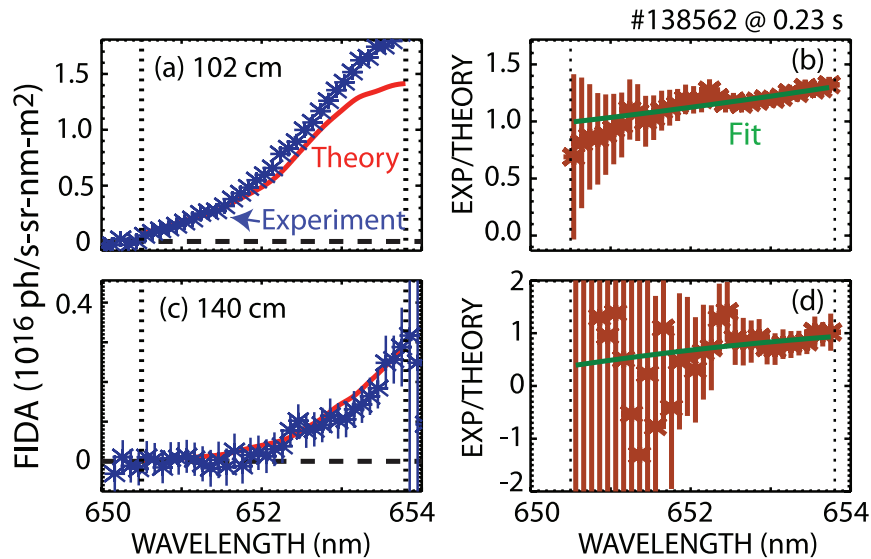
Figure 3. Spectral fitting. Upper (lower) row: case with excellent (marginal) signal-to-noise ratio. (*a*), (*c*) FIDA spectra after subtraction of the passive signals from the active signals. The theoretically predicted spectra are also shown. (*b*), (*d*) Ratio of the measured signal to the predicted signal versus wavelength. The solid lines show the weighted least-squares fits to the spectral ratios. The dotted vertical lines indicate the spectral range for the fits. Note: the absolute value of the experimental data is approximate in this and all subsequent figures.

a negligible contribution to the measurement. The active and passive spectra should coalesce for wavelengths below 649.6 nm and wavelengths above 662.6 nm, as these are the maximum possible Doppler shifts for a 90 keV deuterium atom. (The maximum Stark splitting is <0.2 nm in NSTX so, for a typical case, FIDASIM predicts no signal below 649.8 nm or above 662.4 nm.) As observed previously [18], the blue-shifted spectra satisfy this criterion but the red-shifted spectra do not. Another previous finding is that background subtraction using the reference views is consistent with background subtraction from beam modulation for the blue-shifted side of the spectrum but often deviates for the red-shifted side [18]. Accordingly, the data analyzed here are entirely from the blue-shifted portion of the spectrum. Unfortunately, the absolute intensity calibration is corrupted for both the FIDA and the charge-exchange recombination spectroscopy [19] diagnostics for the 2010 data (possibly owing to a problem with the absolutely calibrated black-body source). The value employed here is consistent with the available information but is too unreliable for a meaningful comparison. The relative channel-to-channel calibration factors rely on a white-plate calibration technique that should be valid, however.

Data processing consists of several steps. The net signal is the difference between the active and reference signals. Since the active and reference views are similar but not identical, the active data are interpolated onto the positions of the reference views. Errors in the net signal are obtained from the photon statistics of the active and reference views. Representative FIDA data appear in figure 3.

To compare with theory, the NUBEAM module [20] of the TRANSP code [21] calculates the fast-ion distribution function. A typical spatially-averaged distribution function is shown in figure 4(*a*). The starting point for this analysis
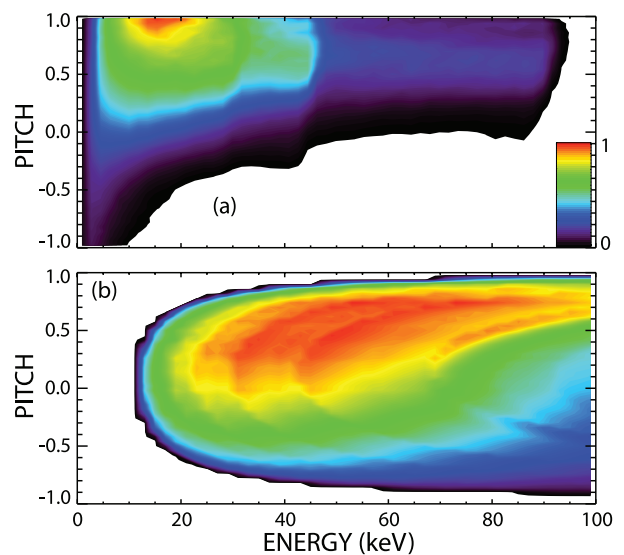
Figure 4. (*a*) Spatially averaged classical fast-ion distribution function calculated by NUBEAM in discharge #140740 at 360 ms. (*b*) Velocity-space sensitivity of the FIDA chord at 122 cm after integration between 650.5 and 653.8 nm for the same shot and time.

is the TRANSP runs prepared for [1]. The NUBEAM option to include *ad hoc* diffusion is turned off, so the predicted distribution functions neglect transport by instabilities. The NUBEAM distribution function is input to the Fortran 90 version [22] of the FIDASIM code [23]. The plasma profiles needed to simulate the FIDA spectra are extracted from the TRANSP output. Instrumental broadening is applied to the FIDA spectra prior to comparison with the data. Figure 3 shows representative comparisons for a case with excellent statistics and a case with a marginal signal-to-noise ratio.
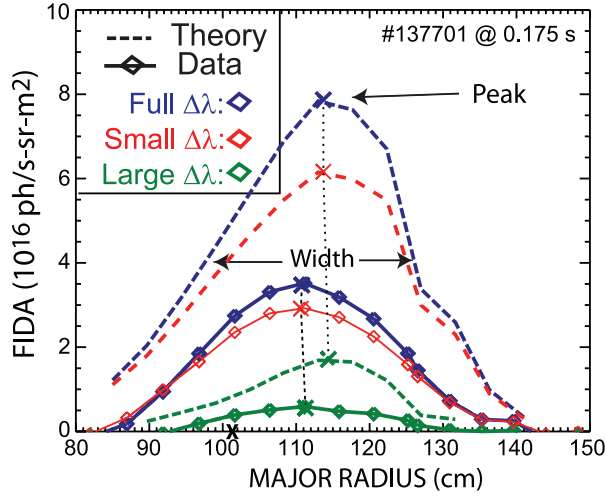
Figure 5. Profile fitting. Theoretical (dashed lines) and experimental (solid lines with diamonds) radial profiles for three different ranges of spectral integration. The lowest-radiance profile is for large Doppler shifts (650.5–652.3 nm), the middle profile is for small Doppler shifts (652.3–653.8 nm) and the largest profile is for the entire spectral range (650.5–653.8 nm). The fitted peaks are marked by an X. The FWHM of the full-energy theoretical profile is also indicated. On this and all subsequent profiles, the magnetic axis is marked on the axis by an X.

Table 1. Left: range of central electron temperature, average electron density, injected beam power, toroidal field, plasma current and central ion temperature in the database. Right: number of cases of each type of MHD activity.

| Parameter	Range	MHD	# Cases
$T_e(0)$	0.5–1.5 keV	ALE	33
$\bar{n}_e$	0.9–7.3×10^{19} m^{-3}	Avalanche	84
P_B	1.5–6.1 MW	TAE	40
B_T	0.21–0.48 T	EPM	72
I_p	0.30–1.11 MA		
$T_i(0)$	0.3–2.1 keV		

Once the calibrated experimental and theoretical spectra are assembled, they are analyzed in several different ways. A useful measure of the quality of the experimental data is to compare with the 'null hypothesis' of zero FIDA emission. The reduced chi-squared for the null hypothesis is

$$\chi^2_{null} = \sum_{i=1}^{N}(s_i/\sigma_i)^2/(N-1) \qquad (1)$$

where s_i and σ_i are the signal and error in each wavelength bin and the sum is over the $N \simeq 70$ wavelength bins between 650.5 and 653.8 nm. This provides a figure of merit that is very useful for eliminating cases with poor signal-to-noise ratios in the subsequent analysis. For example, the signal-to-noise ratio for the spectrum shown in figure 3(a) is excellent; the large value of $\chi^2_{null} = 231$ in this case indicates that the data are incompatible with the null hypothesis. In contrast, the signal-to-noise for the spectrum shown in figure 3(c) is
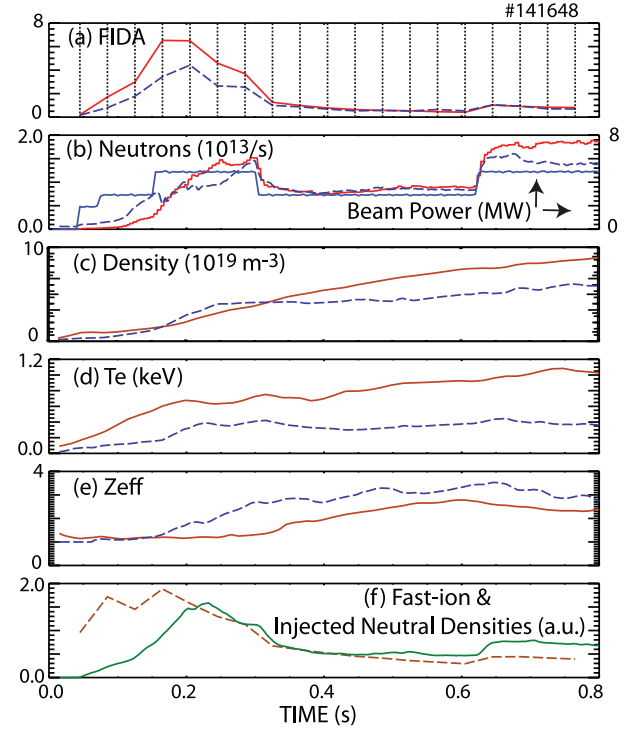

Figure 6. Time evolution of measured and analyzed quantities in a representative discharge. (*a*) Theoretical (solid line) and experimental (dashed line) peak FIDA radiance (10^{16} photons s^{-1} sr^{-1} m^{-2}), (*b*) theoretical (solid line) and experimental (dashed line) neutron rate and beam power, (*c*) electron density at the magnetic axis (solid) and half-radius (dashed), (*d*) electron temperature at the magnetic axis (solid) and half-radius (dashed), (*e*) Z_{eff} at the magnetic axis (solid) and half-radius (dashed), (*f*) TRANSP fast-ion density (solid) and FIDASIM injected-neutral density (dashed) at $R \simeq 115$ cm. The times for the profiles in figure 8 are indicated by the dotted vertical lines.
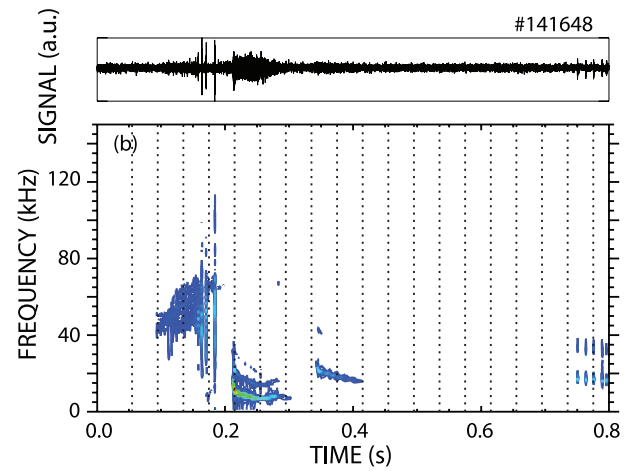
Figure 7. Magnetic (*a*) signal and (*b*) spectrum in the same discharge as figure 6.

relatively poor; the small value of $\chi^2_{null} = 3.8$ in this case suggests that comparisons with theory are of limited utility for this case. In the database results reported below, a condition
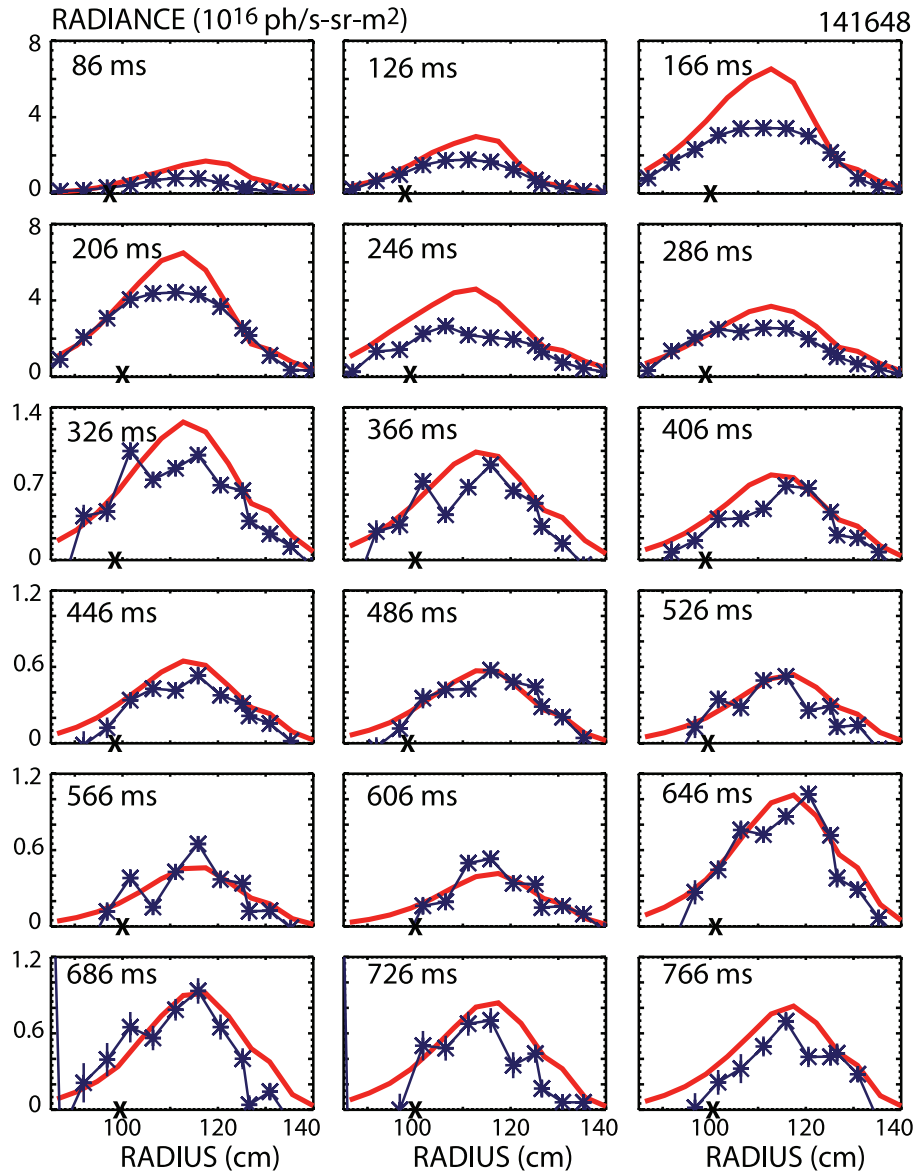
Figure 8. Theoretical (solid) and experimental ($\times$) FIDA profiles versus major radius at 18 different times in the discharge of figure 6.

is excluded if none of the radial channels in the profile has $\chi^2_{\mathrm{null}} > 8$.

The shape of the FIDA spectrum provides information about the energy dependence of the distribution function. Because the Doppler shift depends on only one component of the velocity vector, the actual dependence on energy is complicated and is described by a 'weight function' (or velocity-space sensitivity) [24]. Nevertheless, in a qualitative sense, larger Doppler shifts correspond to higher minimum energies and smaller Doppler shifts to lower minimum energies. The weight function for a typical case after integrating over wavelengths is shown in figure 4(*b*). To search for differences between the predicted and measured spectral shapes, the experimental spectrum is divided by the theoretical spectrum. The normalized spectrum is fitted by a quadratic, including weights associated with photon statistics. The spectrum in

figure 3(*a*) resembles the predicted shape but the data are lower than the prediction at large Doppler shifts and higher at small Doppler shifts (figure 3(*b*)). In the quadratic fit, this difference is reflected in a non-zero value for the linear term. A similar trend is evident for the spectrum in figure 3(*c*) but, in this case, the theory exceeds experiment at most wavelengths (figure 3(*d*)).

Radial profiles are obtained by integrating the spectra over specified wavelength ranges. Most of the analysis employs the full wavelength range shown in figure 3 (650.5–653.8 nm). To test the high-energy and low-energy profiles, respectively, radial profiles are also calculated for large Doppler shifts (650.5–652.3 nm) and small Doppler shifts (652.3–653.8 nm). (These wavelengths correspond to energies associated with the velocity component along the line of sight of 31–68 keV and 11–31 keV, respectively.) An example of these three

profiles for both theory and experiment appears in figure 5. Once the profiles are determined, the location and magnitude of the peak are calculated from a fit to the five channels closest to the maximum; then the half-width of the profile is found. These quantities are stored in the database for the three different wavelength ranges.

To detect changes in spectra and profiles associated with a bursting instability, three successive times are analyzed for each case. The first time precedes the instability burst, the second time includes (or immediately follows) the burst and the third time is the next time bin (during the recovery phase). To guide the use of these three adjacent time periods, classifications such as 'quiet prior to the burst' and 'steady MHD activity throughout the time period' are included in the database.

For the TRANSP runs of [1], this procedure yields 232 cases from 123 shots with usable experimental and theoretical FIDA data. The assembled database also incorporates neutral beam parameters and plasma parameters extracted from TRANSP. Database parameters are summarized in table 1.

3. General trends

Many of the general trends are evident in a single discharge, #141648. This is an H-mode plasma with variations in beam power (figure 6(*b*)) and steadily increasing electron density throughout (figure 6(*c*)). After an initial rapid rise, the electron temperature gradually increases but remains $\lesssim 1$ keV (figure 6(*d*)). This relatively low value implies that, classically, fast ions slow down primarily on electrons with minimal pitch-angle scattering. Throughout the discharge, Z_{eff} steadily rises to a relatively high value of ~ 3 by 0.8 s (figure 6(*e*)). The measured and predicted neutron rates agree well in the middle of the discharge but experiment exceeds theory initially and is smaller than the calculated rate at 0.25 s and again at the end of the discharge (figure 6(*b*)). The temporal evolution of the measured peak FIDA signal generally varies as predicted (figure 6(*a*)), although the rise is smaller than predicted early in the discharge. The FIDA signal is proportional to the product of the injected neutral density and the fast-ion density $n_{inj}n_f$. Largely in response to the rising electron density, in the latter half of the discharge, the injected neutral density in the FIDA sightline and the calculated fast-ion density both decrease (figure 6(*f*)). Earlier in the discharge, the behavior of n_{inj} is more complicated, as reduced penetration due to increasing n_e is compensated by increases in beam power; for n_f, the initial rise in T_e results in a large initial increase in slowing-down time τ_s, which raises n_f.

As is typical in NSTX, discharge #141648 exhibits a wide variety of MHD (figure 7). Between 0.1 and 0.2 s, TAE activity with frequency ~ 60 kHz and dominant mode numbers of $n = 1$ and $n = 2$ predominates. Then, at 0.21 s, a low-frequency $n = 1$ mode is excited that persists for ~ 0.1 s then reappears weakly between 0.34 and 0.40 s. Bursting $n = 1$ 'fishbone' events occur after 0.74 s. Not shown in figure 7 are MHz CAE or GAE fluctuations that occur between 1.5 and 2.0 MHz from 0.2–0.3 s and between 0.5 and 1.0 MHz from 0.6–0.8 s.
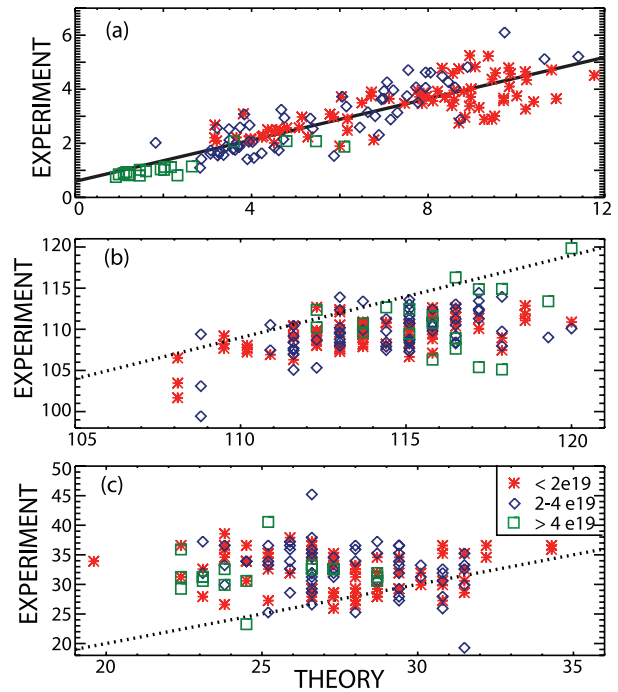
Figure 9. Database results from profile fitting. The symbols represent low ($\times$), moderate ($\Diamond$) and high ($\square$) electron density. (*a*) FIDA radiance at peak. (*b*) Major radius of the profile peak. (*c*) FWHM of the radial profile. The dotted lines represent agreement between theory and experiment; the solid line is a linear fit to the radiance data.

Figure 8 compares theoretical and experimental FIDA profiles at 18 different times in discharge #141648. For much of the discharge, the theoretical prediction is more peaked than the experimental profile. Initially, the theory predicts a peak at larger major radius than is observed experimentally. As the discharge evolves, the peak migrates to larger major radius. This is an expected consequence of rising n_e, which causes more rapid attenuation of the injected neutral density. The decreasing signals with increasing time are also expected, as rising n_e reduces both n_{inj} and n_f. Relative to theory, the measured FIDA intensity is smallest early in the discharge, when the MHD activity is strong.

These trends are generally observed. Overall, the correlation of the measured peak radiance with the predicted peak radiance is strong (Pearson product-moment correlation coefficient $r = 0.88$) (figure 9(*a*)). To search for additional dependences, we consider the ratio of experiment to theory as a function of plasma parameters. The ratio of experiment to theory tends to be smaller in discharges with large fast-ion populations. The strongest correlation in the database ($r = -0.49$) is with the product $P_B\tau_s$ (figure 10(*a*)), a quantity that is proportional to the number of beam ions. The correlation with τ_s alone is also strong ($r = -0.42$), as is the correlation with the ratio of volume-averaged fast-ion beta to volume-averaged plasma beta, β_f/β_T ($r = -0.47$). Conversely, the ratio tends to increase with electron density ($r = 0.31$). Other quantities that depend upon density, such as the ratio of fast-ion speed to
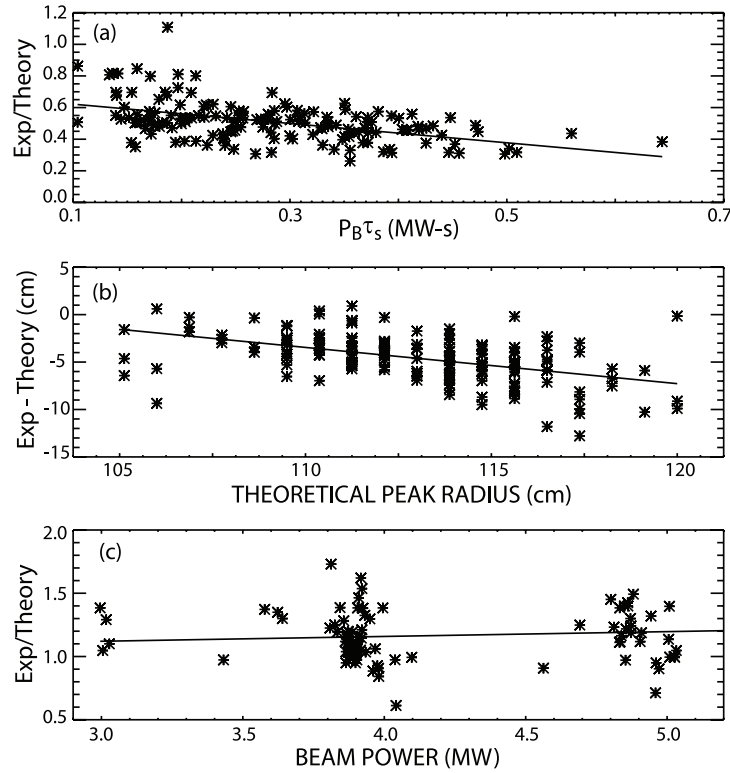
Figure 10. (*a*) Ratio between the experimental peak radiance and the theoretically predicted peak radiance versus the product of beam power and slowing-down time for all of the cases in the database. (*b*) Difference between the measured radius of the FIDA peak and the theoretically predicted peak radius versus the theoretical prediction. (*c*) Ratio between the experimental width of the FIDA profile and the theoretically predicted width versus beam power.

Alfvén speed, v_f/v_A ($r = 0.38$), also correlate with the radiance ratio. The dependence of the ratio on other parameters such as q and I_p is relatively weak. Consideration of the profiles over a more limited spectral range also has little effect.

Experimentally, the radius of the peak signal is generally less than the theoretical prediction (figure 9(*b*)). On average, the experimental peak is at 109.5 cm, while the theoretical peak is at 113.6 cm. The overall correlation of experiment with theory is weaker than for the radiance, $r = 0.56$. The difference between the experimental and theoretical peak positions is insensitive to plasma parameters, with the strongest dependence being on q_{95} ($r = 0.22$). The strongest correlation in the database is with the theoretical prediction itself ($r = -0.48$) (figure 10(*b*)). The experimental profile does not vary as much as theory predicts. The discrepancy is largest when theory predicts a large outward shift of the FIDA profile. This could originate from a loss process that is strongest near the outer edge (such as ripple).

The experimental profile is usually wider than the theoretical profile (figure 9(*c*)). On average, the measured width is 21% greater than predicted but the observed width does not correlate with the theoretical prediction ($r = -0.18$). The difference between theory and experiment is insensitive to all quantities in the database, including plasma and beam parameters and instability type. The strongest correlation of the ratio is with beam power (figure 10(*c*)) but the dependence is weak ($r = 0.19$).

To summarize, the FIDA signal level scales as predicted by theory but the ratio decreases in plasmas with large fast-ion populations, where instability-induced transport is likely. Similar results occur in conventional tokamaks. In the absence of instabilities, comparisons that follow essentially the same calibration and analysis procedure find good agreement between theory and experiment [25, 26], but reductions in the FIDA signal are commonplace in the presence of instabilities driven by fast ions (e.g. [27]).

A difference from conventional tokamaks is the insensitivity of the measured peak radius and profile width to changes in plasma conditions. It is evident from inspection of figures 9(*b*) and (*c*) that the peak radius and profile width are nearly constant, independent of the theoretical prediction. (Quantitatively, in comparison to the best linear fit, a fit to a constant value has a chi-squared that is only 46% higher for the peak radius and 1% higher for the width.) Here, we consider several possible explanations for the invariance of the fast-ion profile.

(1) The experimental channel-to-channel calibration is wrong. This is certainly a possibility but it seems unlikely, as a single recalibration cannot bring the peak location and profile width into agreement with theory for all cases simultaneously.

(2) Errors exist in the plasma parameters that are input to NUBEAM and FIDASIM. The dependence of the
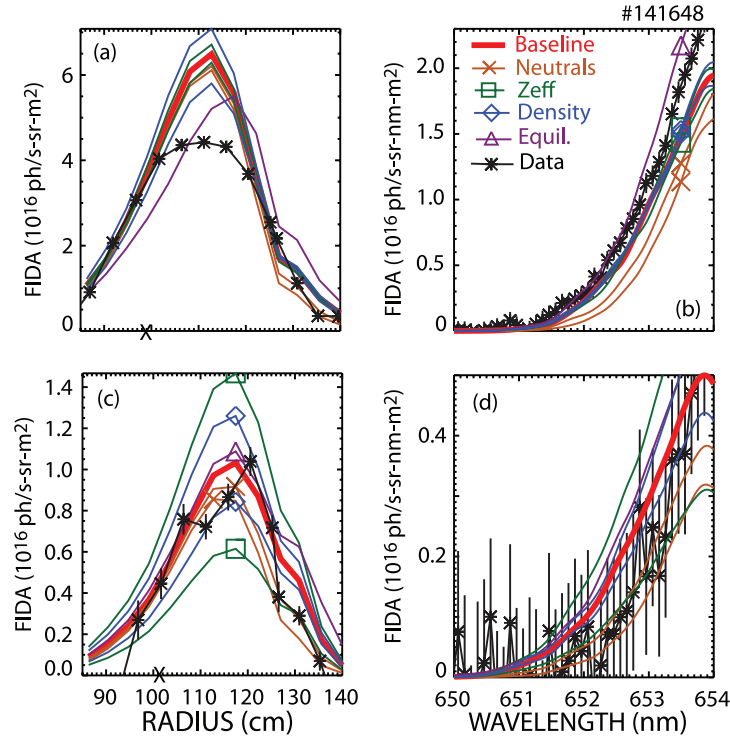
Figure 11. ((*a*), (*c*)) Radial FIDA profiles and ((*b*), (*d*)) FIDA spectra for the channel at $R = 125$ cm at two different times in the discharge of figure 6. The baseline theoretical prediction (thick solid line) is modified by (X) increasing the edge neutral density by a factor of 10 or 100, by (□) raising and lowering Z_{eff} by 25%, by (◇) raising and lowering n_e by 10%, and by (△) repeating the calculations with LRDFIT equilibria.

Table 2. Average effect of parameter changes on the FIDASIM profile for 14 time slices in discharge #141648.

| Parameter	Intensity	Radius	Width
$10n_0$	0.93	1.00	0.94
$100n_0$	0.89	0.99	0.92
$0.75Z_{eff}$	1.19	1.00	1.00
$1.25Z_{eff}$	0.82	1.00	1.02
$0.9n_e$	1.14	1.00	0.99
$1.1n_e$	0.88	1.00	1.01
Equilibria	0.98	1.01	1.06

Note: The fractional change in the peak intensity, major radius and FWHM relative to the baseline are listed.

theoretical predictions on plausible uncertainties in the input data is considered for discharge #141648 (figure 6) in figure 11 and table 2.

(a) One possibility is that charge-exchange losses are underestimated. A difference between conventional and spherical tokamaks is the large fast-ion gyroradius. Figure 12 show some representative orbits. Perhaps the $\sim$15 cm gyroradius leads to enhanced charge-exchange losses, as ions on drift orbits that approach the edge traverse the high neutral-density edge region. This effect could account for the tendency of the experimental profile to peak at smaller major radius than theoretically predicted (figure 9(*b*)). To investigate this hypothesis, new TRANSP calculations are performed with enhanced edge neutral
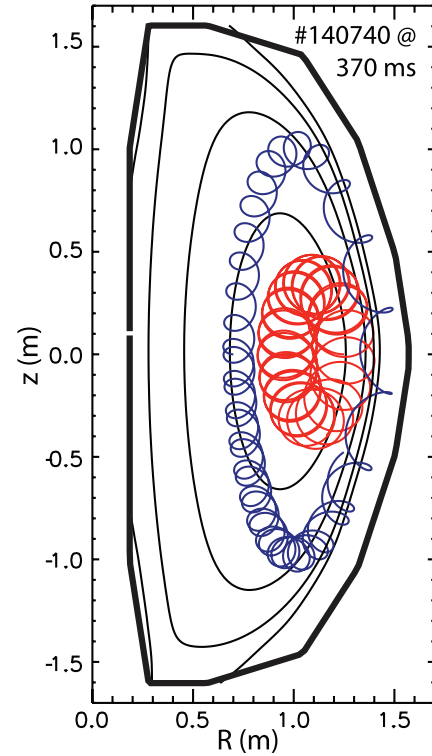
Figure 12. Orbits of 90 keV ions with pitch of $v_\parallel/v = 0.40$ and 0.71 in a typical equilibrium.
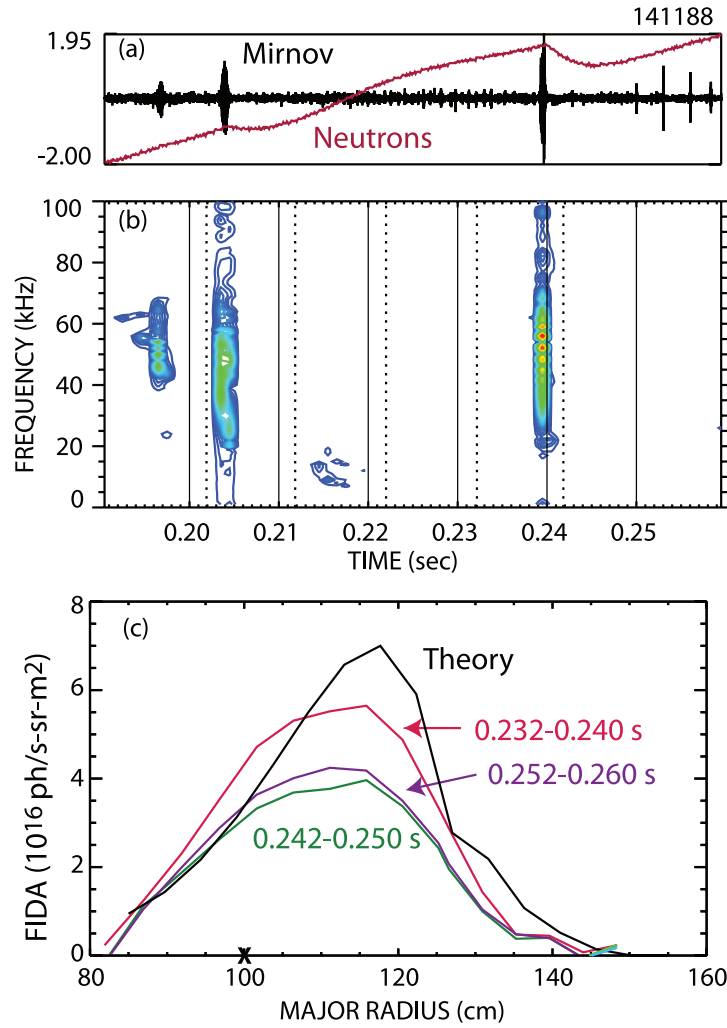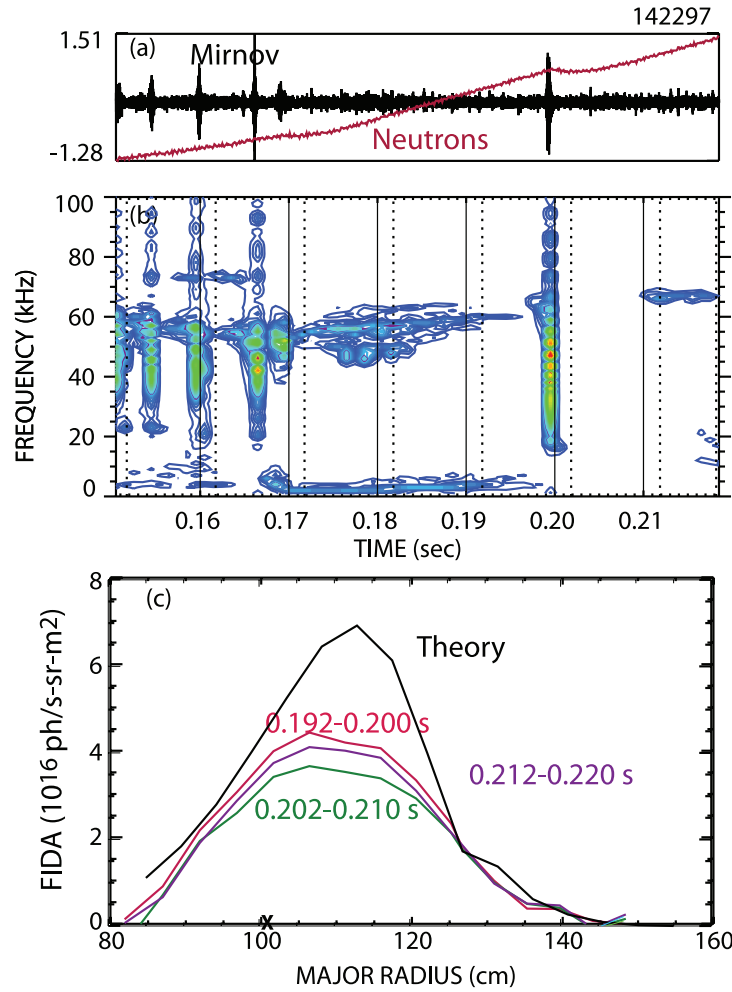
Figure 13. Effect of an ALE on the FIDA profile. (*a*) The ALE occurs at 0.239 s and causes a 9% reduction in neutron emission. (*b*) Magnetics spectrum. The integration windows for the CCD camera fall between the solid and dotted vertical lines. (*c*) FIDA profiles just before (0.232–0.240 s), immediately after (0.242–0.250 s) and during recovery (0.252–0.260 s) from the ALE event. The theoretical profile is also shown.
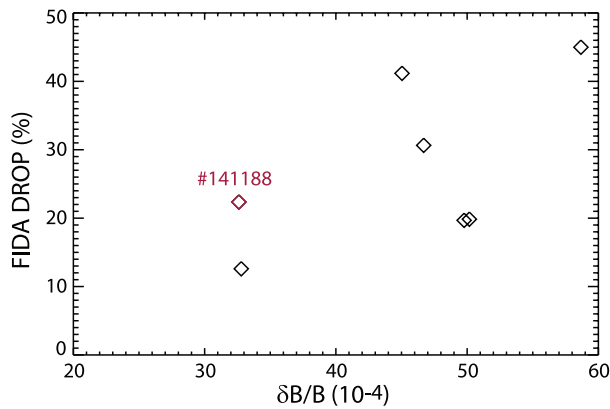
Figure 14. Drop in peak FIDA signal versus amplitude of the ALE burst. The point associated with the case shown in figure 13 is indicated.

density. Increasing the neutral density by two orders of magnitude decreases the predicted profile width without appreciably shifting the location of the peak (table 2), so this is unlikely to account for the discrepancy. Moreover, an experimental argument against this hypothesis is the observation that, for the database, the experimental width does not correlate with the toroidal field.

(b) Uncertainties in Z_{eff} are another plausible source of error. To investigate the sensitivity to Z_{eff}, the TRANSP and FIDASIM calculations are repeated with the measured carbon profile $n_c(r)$ multiplied by factors of 1.25 and 0.75. (The baseline TRANSP runs utilize the carbon density measured through charge-exchange recombination spectroscopy [19] and assume that carbon is the principal impurity in the plasma. The estimated uncertainty in Z_{eff} is ±5% in low-density plasmas, rising to ±15% in high-density H-mode plasmas where beam attenuation is

Figure 15. Effect of a TAE avalanche on the FIDA profile. (*a*) The avalanche occurs at 0.199 s and causes a 2–3% reduction in neutron emission. (*b*) Magnetics spectrum. The integration windows for the CCD camera fall between the solid and dotted vertical lines. (*c*) FIDA profiles just before (0.192–0.200 s), immediately after (0.202–0.210 s) and during recovery (0.212–0.220 s) from the avalanche event. The theoretical profile is also shown.

strong.) Owing to quasineutrality, changes in carbon density alter the calculated thermal deuterium density n_d and, thereby, alter the calculated halo density n_{halo}. The effect is greatest later in the discharge when Z_{eff} is relatively large (figure 6(*e*)). Consequently, increased Z_{eff} lowers the predicted FIDA radiance (figure 11(*c*)). (At higher density, changes in Z_{eff} also alter the atomic energy occupation levels but this is a smaller effect.) Although the assumed value of Z_{eff} has a strong effect on the predicted intensity, the impact on the predicted radius and width of the profile is weak (table 2).

(*c*) It is well known that the FIDA signal depends sensitively on the electron density [25]; however, systematic errors in n_e for the NSTX Thomson scattering diagnostic [28] are thought to be rather small, $\lesssim$10%. Rescaling the measured density profile by ±10% alters the predicted intensity but has only a slight effect on the predicted radius and width of the FIDA profile (table 2).

(*d*) Errors in T_e or P_B are unlikely to explain the profile discrepancy. One check on the calculated distribution

function is to compare the measured neutron rate with the TRANSP prediction. On average, the measurement is 82 ± 27% of the theoretical prediction; in nearly 20% of the cases, the measured rate exceeds the prediction. In light of the strong MHD activity in many of the discharges, an average reduction in neutron rate relative to the prediction is expected. The fact that the measured neutron rate exceeds the prediction for many of the cases argues against a systematic overestimate of T_e or P_B.

(*e*) The biggest impact on the predicted profile is associated with the selected equilibria. Most of the TRANSP runs for the database utilize EFIT [29] equilibria that use magnetics and motional Stark effect data. For comparison, the TRANSP and FIDASIM predictions are repeated for discharge #141648 using equilibria that are generated by a fitting code [30] that utilizes magnetics and T_e isosurfaces. The choice of equilibrium alters the profile (figure 11(*a*)), especially early in the discharge when the q profile is reversed; however, the predicted profile shifts outward, in poorer agreement with experiment.
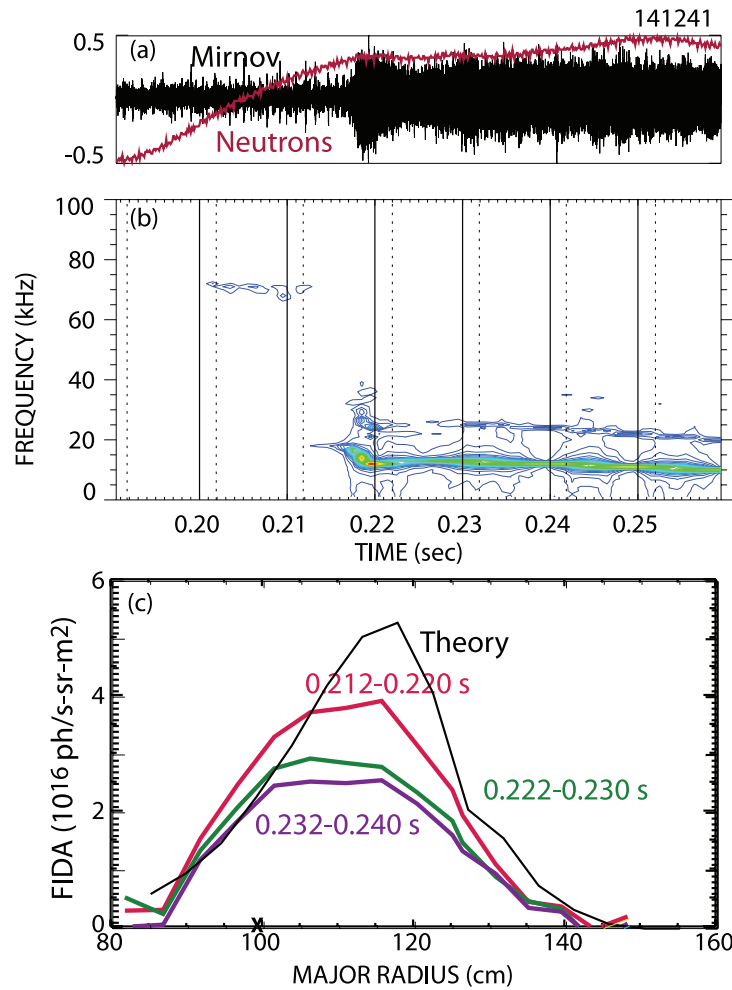
Figure 16. Effect of the onset of an EPM on the FIDA profile. (*a*) The mode begins at 0.218 s and causes a change in slope of the neutron emission. (*b*) Magnetics spectrum. The integration windows for the CCD camera fall between the solid and dotted vertical lines. (*c*) FIDA profiles just before (0.212–0.220 s), immediately after (0.222–0.230 s) and during the subsequent $n = 1$ mode (0.232–0.240 s). The theoretical profile is also shown.

On average, the peak location is unaffected but the width of the profile increases by 6% (table 2), in better agreement with experiment.

Figures 11(*b*) and (*d*) show the effect of changes in input parameters on the predicted spectrum for a single FIDA channel. Fitting the spectral shape for the various cases shows that the fit coefficients (figure 3) are sensitive to the assumed variations for this and other FIDA channels. This sensitivity probably accounts for the large variations in spectral fit coefficients observed experimentally.

In conclusion, although the theoretical calculations are sensitive to uncertainties in plasma parameters, it seems unlikely that these effects account fully for the weak sensitivity of the FIDA profile to plasma conditions.

 (3) The relatively large orbits (figure 12) may not be accurately modeled in NUBEAM or FIDASIM. Although the drift-orbit effects in these codes have been extensively tested in conventional tokamaks (e.g. in [31]), spherical tokamaks have very large gyroradii that could be improp-

erly treated. A comparison of vertical FIDA data from the MAST spherical tokamak with predictions based on NUBEAM and FIDASIM also revealed possibly discrepancies [12].

(4) The compressional and global Alfvén eigenmodes that are present in most NSTX discharges alter the FIDA profile by redistributing the fast ions in phase space. It was previously suggested that these modes impact the thermal ion power balance [32] (although subsequent study suggests this is unlikely [33]) and it was found that GAEs correlate with an unusual enhancement in the measured neutral-particle spectrum when TAEs are absent [34]. Since fast ions interact with these MHz waves through a Doppler-shifted cyclotron resonance, interactions with CAEs and GAEs could reduce the perpendicular fast-ion velocity, thereby altering the intensity of the FIDA light from a vertical view. To investigate this hypothesis, magnetics signals are analyzed within ± 10 ms for all of the times in the database. The peak and rms amplitudes are recorded in two frequency
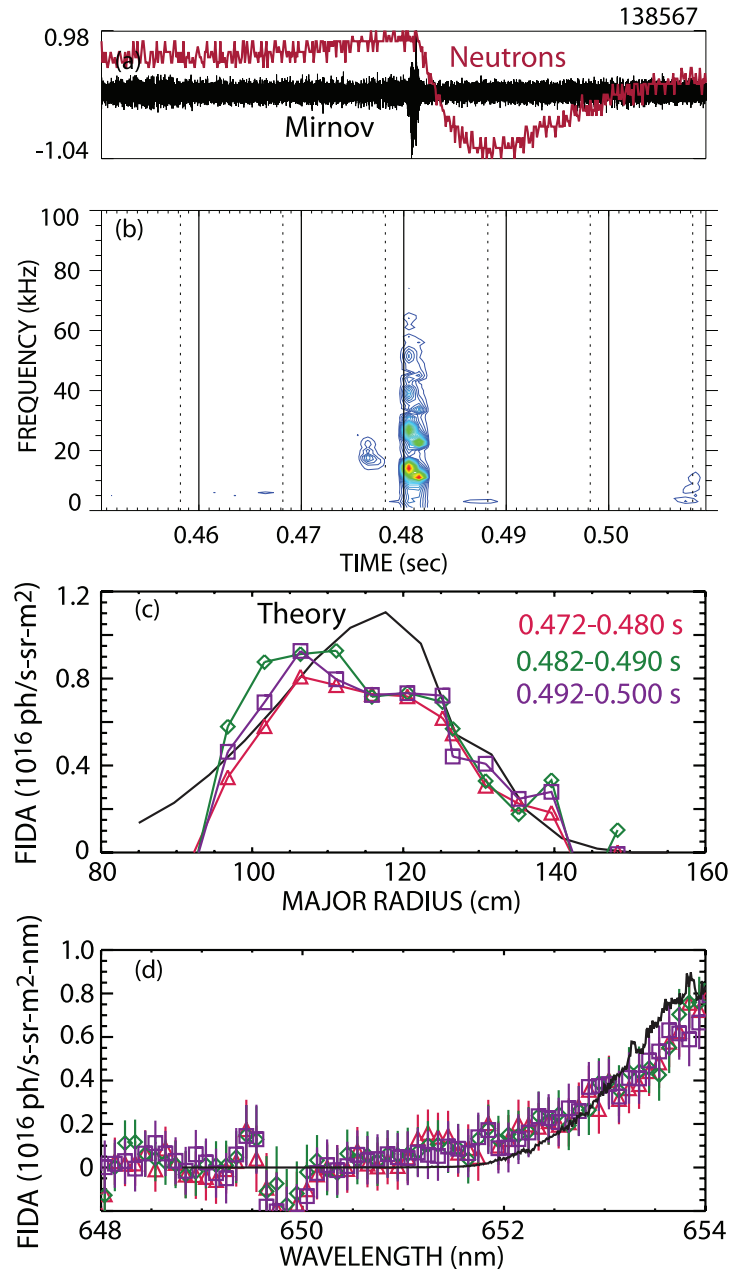
Figure 17. Effect of a fishbone on the FIDA profile. (*a*) The mode begins at 0.48 s and causes a 19% drop in the neutron emission. (*b*) Magnetics spectrum. The integration windows for the CCD camera fall between the solid and dotted vertical lines. (*c*) FIDA profiles just before (0.472–0.480 s, triangle symbols), immediately after (0.482–0.490 s, diamond) and during the recovery phase (0.492–0.500 s, square). The theoretical profile (line) is also shown. (*d*) Spectra for the same three times for the channel at $R = 125$ cm. The error bars represent photon statistics.

bands: 0.3–1.5 MHz (nominal GAE band) and 1.5–2.5 MHz (nominal CAE band). The correlation of these four signals with the ratio of measured-to-predicted FIDA intensity or measured-to-predicted FIDA width is weak; the strongest correlation is between the 'GAE' rms amplitude and the FIDA intensity ratio ($r = 0.30$). This analysis suggests that the MHz modes are not the primary cause of the discrepancy.

(5) An unidentified process redistributes the fast ions and flattens the FIDA profile in most NSTX discharges.

Perhaps a persistent mode exists that is undetected by the magnetics. Perhaps fast-ion transport by electromagnetic turbulence is more important in a high-beta spherical tokamak than it is in a conventional tokamak. Perhaps error fields scatter fast ions with orbits that traverse the edge region. As a rough estimate of the requisite transport magnitude, a simulation with spatially uniform diffusion coefficient of $D_B = 1.0$ m^2 s^{-1} broadens the profile to a width of $\sim$35 cm, indicating that anomalous transport of this magnitude is required.
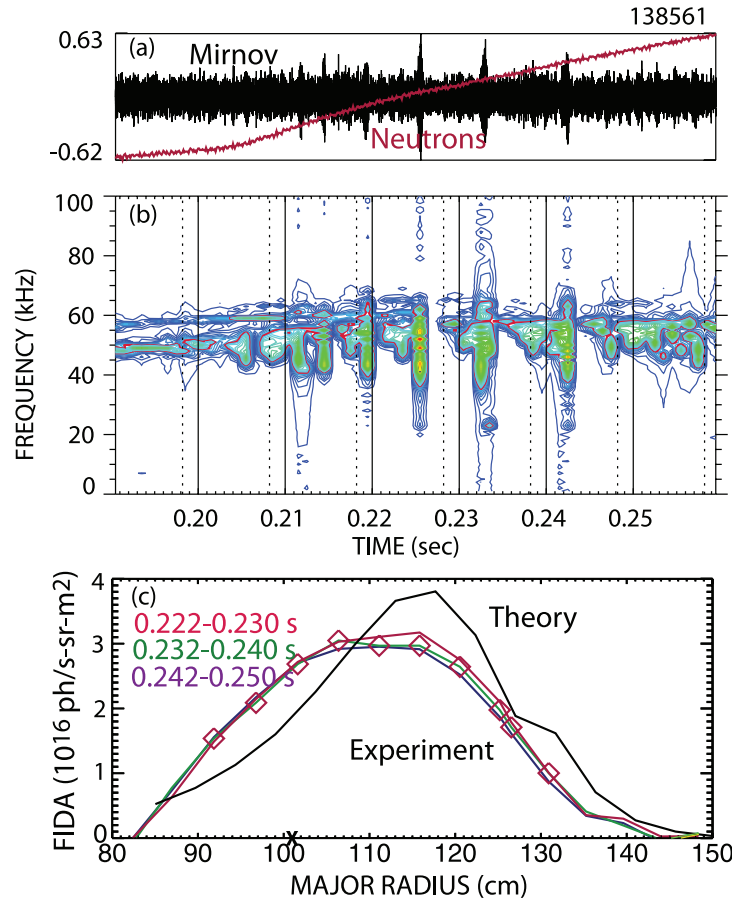
Figure 18. (*a*) Neutron rate and magnetics signal and (*b*) magnetics spectra in a discharge with persistent, bursting TAE activity. The integration windows for the CCD camera fall between the solid and dotted vertical lines. (*c*) FIDA profiles for three adjacent time slices between 0.222 and 0.250 s. (The profiles are nearly identical.) The theoretical profile is also shown.
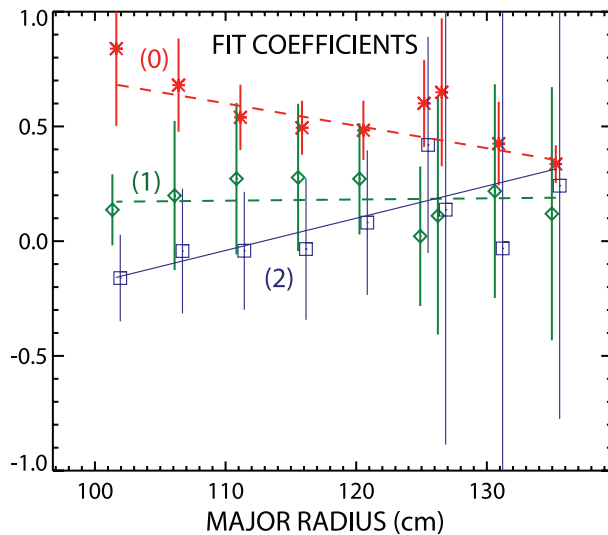
Figure 19. Fitting coefficients versus major radius for all of the slices with persistent TAE activity in the database. The error bars represent the standard deviation of the binned data. The dashed lines are linear fits to the binned data for the constant (∗), linear (◊) and quadratic (□) terms in the spectral fit.

4. Dependence on the type of MHD

An MHD burst can alter the fast-ion profile. Unfortunately, the relatively long camera exposure time of ∼8.1 ms often complicates the analysis of rapidly evolving distribution functions. For a subset of cases, the MHD event occurs near the end of a time bin or during camera readout (when the light is blocked). If the ∼10 ms prior to the event is free of appreciable MHD, comparison of the profiles before and after the event provides an unambiguous measurement of the effect of the event on the fast-ion profile.

The seven ALE events that satisfy these selection criteria all cause reductions in FIDA signal across the entire radial profile. The 29% drop shown in figure 13 is typical. This reduction is *not* caused by changes in plasma parameters; for example, for these seven events, the electron temperature measured by Thomson scattering is $(2 \pm 3)\%$ *larger* in the time slice immediately following the event. The reduction occurs approximately uniformly across the radial profile. Examination of the spectral fit coefficients shows that the spectral shape remains similar after the event. Apparently, the ALE causes reductions in fast-ion confinement throughout phase space. For this set of events, the magnitude of the FIDA reduction scales with

the size of the MHD event as measured by a magnetic coil on the outer wall (figure 14.) The average FIDA reduction for these events (27%) is similar to the average neutron reduction (24%), which is consistent with the hypothesis that the losses occur in a wide swath of phase space.

The effect of TAE avalanches on the FIDA profile is similar (figure 15). In this case, not every event that satisfies the selection criteria reduces the profile, but the majority do. As for the ALE, the reduction occurs across the profile without appreciable alteration of the spectral shape. In measurements of losses produced by TAE avalanches, Darrow *et al* found that the losses occur for a broad swath of pitch angles [35], in qualitative agreement with these FIDA results.

The onset of an LLM usually causes a reduction in the FIDA profile that persists in subsequent time bins (figure 16). Spatially, the reduction occurs throughout the profile. The spectral shape remains similar before and after the onset of the LLM.

In the majority of cases, reductions in the FIDA signal at fishbones are undetectable. Figure 17 shows a representative example. The fishbones generally occur later in the discharge when the plasma density is relatively high and the FIDA signal is relatively weak. For a set of five similar fishbones with appropriate timing of the FIDA timing windows and average neutron drops of $(20 \pm 3)\%$, the drop is FIDA signal is $(-6 \pm 8)\%$.

Normally, the period between TAE bursts is shorter than 10 ms. Thus, in this case, it is not possible to observe profiles prior to the persistent TAEs. Figure 18 shows a representative case. As expected, under these rather steady conditions, the experimental profiles hardly change in adjacent time bins (figure 18(*c*)). Compared to the theoretical prediction, the experimental profile is wider, has lower peak intensity than usual and is shifted inward in major radius.

Overall, for the discharges with persistent TAE activity, the spectral shape is in approximate agreement with the theoretical prediction. The example shown in figure 3 shows a case with modest disagreement: when plotted versus wavelength, there is a linear trend to the ratio of experiment to theory. This is not the case for all cases with persistent TAE activity, however. Figure 19 shows the fit coefficients (figure 3) as a function of major radius for all of the discharges with persistent TAE activity. Within the errors, the coefficients for the linear and quadratic terms are close to zero. This indicates that, on average, the spectral shape in consistent with theory for these discharges.

5. Conclusion

Analysis of the assembled database yields the following conclusions.

1. There is a systematic discrepancy between the theoretically predicted radial profile and experiment (figure 9). The experimental profile peaks at smaller major radius and is wider than theory predicts.

2. ALE events and TAE avalanches cause reductions in FIDA light (figures 13 and 15). The modest changes in profile and spectral shape suggest that the losses occur in a wide range of phase space.

3. The onset of an $n = 1$ EPM often causes significant reductions in FIDA light (figure 16).

Further investigation of all of these issues in NSTX-Upgrade [36] is anticipated. Data from a tangentially viewing FIDA diagnostic [37] and from solid-state neutral particle analyzer arrays [38] will augment the vertical FIDA and neutron data analyzed here. The complementarity of the different fast-ion diagnostics will help pinpoint the portion of phase space responsible for any discrepancies. Experiments at higher magnetic fields will assess the importance of effects due to finite gyroradius.

References

[1] Fredrickson E.D. *et al* 2014 *Nucl. Fusion* **54** 093007
[2] Shinohara K. *et al* 2001 *Nucl. Fusion* **41** 603
[3] Wong K.L. *et al* 1991 *Phys. Rev. Lett.* **66** 1874
[4] Heidbrink W.W., Strait E.J., Doyle E., Sager G. and Snider R.T. 1991 *Nucl. Fusion* **31** 1635
[5] Podestà M. *et al* 2009 *Phys. Plasma* **16** 056104
[6] Crocker N.A. *et al* 2013 *Nucl. Fusion* **53** 043017
[7] Fredrickson E.D. *et al* 2001 *Phys. Rev. Lett.* **87** 145001
[8] Fredrickson E.D. *et al* 2012 *Nucl. Fusion* **52** 043001
[9] Fredrickson E.D. *et al* 2003 *Phys. Plasma* **10** 2852
[10] Fredrickson E., Chen L. and White R. 2003 *Nucl. Fusion* **43** 1258
[11] Gryaznevich M.P. *et al* 2008 *Nucl. Fusion* **48** 084003
[12] Michael C.A. *et al* 2013 *Plasma Phys. Control. Fusion* **55** 095007
[13] Turnyanskiy M. *et al* 2013 *Nucl. Fusion* **53** 053016
[14] Cecconello M. *et al* 2012 *Nucl. Fusion* **52** 094015
[15] Cecconello M. *et al* 2015 *Plasma Phys. Control. Fusion* **57** 014006
[16] Podestà M., Heidbrink W.W., Bell R.E. and Feder R. 2008 *Rev. Sci. Instrum.* **79** 10E521
[17] Heidbrink W.W. 2010 *Rev. Sci. Instrum.* **81** 10D727
[18] Heidbrink W.W. *et al* 2012 *Rev. Sci. Instrum.* **83** 10D903
[19] Bell R.E. and Feder R. 2010 *Rev. Sci. Instrum.* **81** 10D724
[20] Pankin A., McCune D., Andre R., Bateman G. and Kritz A. 2004 *Comput. Phys. Commun.* **159** 157
[21] Budny R.V. 1994 *Nucl. Fusion* **34** 1247
[22] Geiger B. 2013 Fast-ion transport studies using FIDA spectroscopy at the ASDEX Upgrade tokamak *PhD Thesis* Ludwig-Maximilians-Universität München
[23] Heidbrink W.W., Liu D., Luo Y., Ruskov E. and Geiger B. 2011 *Commun. Comput. Phys.* **10** 716
[24] Salewski M. *et al* 2014 *Plasma Phys. Control. Fusion* **56** 105005

[25] Luo Y., Heidbrink W.W., Ruskov E., Burrell K.H. and Solomon W.M. 2007 *Phys. Plasmas* **14** 112503
[26] Geiger B. *et al* 2011 *Plasma Phys. Control. Fusion* **53** 065010
[27] Heidbrink W.W. *et al* 2007 *Phys. Rev. Lett.* **99** 245002
[28] LeBlanc B.P. 2008 *Rev. Sci. Instrum.* **79** 10E737
[29] Lao L.L., St. John H., Stambaugh R.D., Kellman A.G. and Pfeiffer W.P. 1985 *Nucl. Fusion* **25** 1611
[30] http://w3.pppl.gov/~jmenard/software/lrdfit/lrdfit-index.htm
[31] Heidbrink W.W. *et al* 2012 *Nucl. Fusion* **52** 094005

[32] Gates D.A., Gorelenkov N.N. and White R.B. 2001 *Phys. Rev. Lett.* **87** 205003
[33] Fredrickson E.D. *et al* 2002 *Phys. Plasma* **9** 2069
[34] Medley S.S. *et al* 2012 *Nucl. Fusion* **52** 013014
[35] Darrow D.S. *et al* 2013 *Nucl. Fusion* **53** 013009
[36] Menard J. *et al* 2012 *Nucl. Fusion* **52** 083015
[37] Bortolon A., Heidbrink W.W. and Podestà M. 2010 *Rev. Sci. Instrum.* **81** 10D728
[38] Liu D. *et al* 2014 *Rev. Sci. Instrum.* **85** 11E105